energies

Article

Molecular Dynamics Simulation on the Mechanism of Shale Oil Displacement by Carbon Dioxide in Inorganic Nanopores

Chengshan Li [1], Hongbo Xue [1], Liping Rao [1], Fang Yuan [1], Zhongyi Xu [1], Tongtong He [1], Chengwei Ji [1], Zhengbin Wu [2,*] and Jiacheng Yan [3]

[1] Ninth Oil Production Plant, Changqing Oilfield Branch, China National Petroleum Corporation, Xi'an 710018, China; lichengs_cq@petrochina.com.cn (C.L.); xuehb302@163.com (H.X.); raolp_cq@petrochina.com.cn (L.R.); yuanfang_cq@petrochina.com.cn (F.Y.); xzy_cq@petrochina.com.cn (Z.X.); hulie98573@sina.com (T.H.); jicw_cq@petrochina.com.cn (C.J.)
[2] Hubei Provincial Key Laboratory of Oil and Gas Exploration and Development Theory and Technology, China University of Geosciences, Wuhan 430074, China
[3] School of Earth Sciences, Yangtze University, Wuhan 430100, China; dengjieqc8573@sina.com
* Correspondence: wuzb@cug.edu.cn

Abstract: Shale oil reservoirs feature a considerable number of nanopores and complex minerals, and the impact of nano-pore confinement and pore types frequently poses challenges to the efficient development of shale oil. For shale oil reservoirs, CO_2 flooding can effectively lower crude oil viscosity, enhance reservoir physical properties, and thereby increase recovery. In this paper, the CO_2 displacement process in the nanoscale pores of shale oil was simulated through the molecular dynamic simulation method. The performance disparity of quartz and calcite slit nanopores was discussed, and the influences of nanoscale pore types and displacement rates on CO_2 displacement behavior were further analyzed. The results demonstrate that the CO_2 displacement processes of different inorganic pores vary. In contrast, the displacement efficiency of light oil components is higher and the transportation distance is longer. Intermolecular interaction has a remarkable effect on the displacement behavior of CO_2 in nanopores. On the other hand, it is discovered that a lower displacement rate is conducive to the miscible process of alkane and CO_2 and the overall displacement process of CO_2. The displacement efficiency drops significantly with the increase in displacement velocity. Nevertheless, once the displacement speed is extremely high, a strong driving force can facilitate the forward movement of alkane, and the displacement efficiency will recover slightly.

Keywords: shale oil; carbon dioxide; molecular dynamics simulation; nanopores; displacement characteristics

check for updates

Academic Editor: Reza Rezaee

Received: 25 November 2024
Revised: 27 December 2024
Accepted: 5 January 2025
Published: 9 January 2025

Citation: Li, C.; Xue, H.; Rao, L.; Yuan, F.; Xu, Z.; He, T.; Ji, C.; Wu, Z.; Yan, J. Molecular Dynamics Simulation on the Mechanism of Shale Oil Displacement by Carbon Dioxide in Inorganic Nanopores. *Energies* **2025**, *18*, 262. https://doi.org/10.3390/en18020262

Copyright: © 2025 by the authors. Licensee MDPI, Basel, Switzerland. This article is an open access article distributed under the terms and conditions of the Creative Commons Attribution (CC BY) license (https://creativecommons.org/licenses/by/4.0/).

1. Introduction

China holds an abundance of shale oil resources, making it a crucial sector for increasing domestic crude oil reserves and production. Shale reservoirs are characterized by the extensive development of nanopores, which exhibit low permeability, low porosity, and high heterogeneity [1,2]. This unique microscopic pore structure causes the micro-scale flow of oil and water and the development mechanisms in shale reservoirs to differ significantly from conventional reservoirs. Field experiments and engineering applications have shown that CO_2 can effectively recover oil and gas resources from shale reservoirs, achieving significant production enhancement [3–6]. Under reservoir conditions, CO_2 exists in a supercritical state, possessing a density similar to that of a liquid while maintaining a

viscosity close to that of a gas. This highly diffusive property allows CO_2 to penetrate pores larger than its molecular diameter (0.33 nm), thereby enabling it to mobilize residual oil trapped in the deep nanopores of shale reservoirs through energy enhancement, viscosity reduction, and miscibility mechanisms. This makes CO_2 injection a practical choice for enhancing oil recovery in shale formations [7,8].

Due to the nanoscale characteristics of shale reservoirs, the interactions between fluids and micropore walls become significantly intensified within confined spaces, resulting in variations in the presence of crude oil on shale reservoir surfaces. This, in turn, affects the microscopic displacement processes of CO_2 [9,10]. Currently, experimental challenges in preparing and characterizing specimens for fluid flow in nanopores—alongside the high precision required in measurement and substantial experimental error—limit the consistency and reproducibility of results [11]. The analysis of experimental findings often relies on hypothetical models, and due to the inherent difficulties encountered in experiments, as well as the significant influence of rock walls on fluid flow within nanopores, it is critical to minimize artificial assumptions regarding solid–liquid interactions in simulations. Molecular dynamics (MD) simulations offer unique advantages in this respect, as it can explore fluid flow behavior on a molecular scale without needing conventional assumptions, relying instead on well-established potential energy interaction models in physics [12–14]. With advancements in high-performance computing, the challenges associated with the high computational demand and slower computation speed of MD simulations are being addressed. The adsorption strength of CO_2 and crude oil components on rock surfaces plays a crucial role in determining crude oil mobility and CO_2 displacement efficiency [15]. Previous studies have examined the flow behavior of single-component light alkanes (with carbon numbers less than 10) within nanopores, as well as the effectiveness of CO_2 in enhancing recovery from such systems [16–19].

In most studies, shale oil is often simplified as a single-component oil model, which significantly differs from the actual composition of shale oil. Moreover, another critical factor influencing shale oil displacement behavior, the type of nanopore, also requires further investigation. To address these issues, this study employs three alkane molecules (C_4, C_{12}, C_{20}) to simulate the composition of shale oil through proportional mixing, aiming to investigate the mechanisms of CO_2 static dissolution and the dynamic displacement of crude oil within nanopores. By using equilibrium molecular dynamics simulations, the swelling characteristics of crude oil in a CO_2 system within narrow slits are examined, along with the effects of varying CO_2 concentrations. Additionally, non-equilibrium molecular dynamics simulations are conducted to study the CO_2 displacement of shale oil, thereby revealing the underlying mechanisms of CO_2-driven oil displacement in shale reservoirs.

2. Model Construction

2.1. Model Parameters

The primary mineral composition of the Lucaogou shale oil reservoir in the Jimsar Sag, Xinjiang oilfield consists of quartz, feldspar, and carbonate rocks primarily composed of calcite [20]. Based on this, a quartz and calcite fracture model is constructed in this study. Molecular dynamics simulations are conducted using the NVT ensemble (namely canonical ensemble, under which condition the molecule number, volume, and temperature are determined) radial simulation in the LAMMPS (Large-scale Atomic/Molecular Massively Parallel Simulator) software (Version 2020), with the OPLS (Optimized Potentials for Liquid Simulations) force field selected. The monomers of quartz and calcite are constructed using monomers from the MS database. The crystal parameters for α-quartz are a, b, and c at 0.499, 0.499, and 0.546 nm, respectively, with angular parameters α, β, and γ at 90°, 90°, and 99°, and the ClayFF force field is applied. The crystal parameters for calcite are a, b, and c at

0.499, 0.499, and 1.706 nm, respectively, with angular parameters α, β, and γ at 90°, 90°, and 120°, and the OPLS force field is selected. The α-quartz crystal uses the (1 0 0) plane, and the structure is expanded after hydroxylation saturation. The calcite wall plane uses the (1 0 4) plane and undergoes expansion. A fracture model is created by leaving a 40 Å gap between two parallel substrates perpendicular to the *Z*-axis, with the constructed rock wall plane as the matrix. The fracture space is filled with a certain amount of shale oil molecules, where the shale oil components are represented by a mixture of alkanes, including C_4, C_{12}, and C_{20}, mixed in mass fractions of 5%, 45%, and 50%, respectively [21,22].

For the construction of the swelling model, a specified number of alkane molecules are added as the oil component within the fracture, and the system is filled under conditions of 330 K and 40 MPa temperature and pressure. After the filling process, dynamic equilibration is performed for 2 ns. Following equilibration, different concentrations of CO_2 are introduced around the oil components. This configuration serves as the initial model for the swelling process, with the corresponding models depicted in Figure 1.

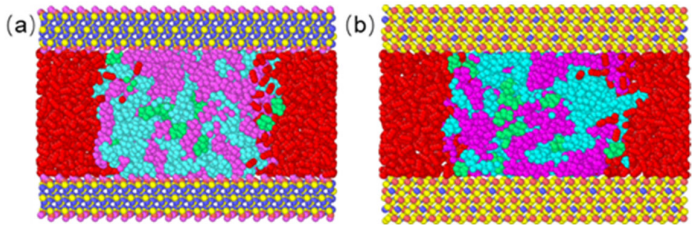


Figure 1. Initial state diagrams of the swelling model: (**a**) quartz slit model, and (**b**) calcite slit model. (Red represents CO_2, green represents C_4, blue represents C_{12}, and purple represents C_{20}).

For the construction of the displacement model, an alkane mixture was used as the oil phase and filled to the left of the slit centerline under temperature and pressure conditions of 330 K and 40 MPa. On the left side of the slit model, a CO_2 atmosphere was introduced under the same temperature and pressure conditions. A rigid pressure plate was positioned on the left side of the CO_2 system to set different displacement velocities, thereby providing the driving force for the CO_2 system. Finally, a vacuum layer with a certain spatial extent was added to the right side of the overall model to eliminate periodicity along the *X*-axis. A detailed model diagram is shown in Figure 2.

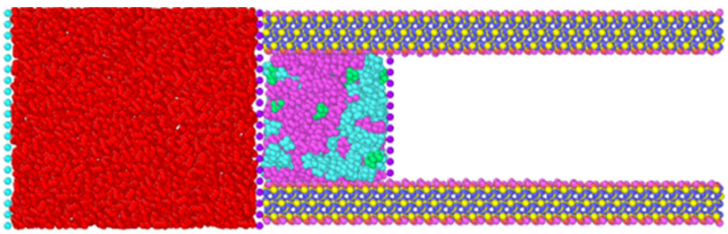


Figure 2. Schematic diagram of the initial construction of the slit displacement model (with red representing CO_2, green representing C_4, blue representing C_{12}, and purple representing C_{20}).

2.2. Model Methodology and Details

The force field component in molecular dynamics simulations primarily involves van der Waals interactions, Coulombic electrostatic interactions, bond stretching, bond angle variations, dihedral torsion, and coupling effects, all of which contribute to the system's total potential energy. To ensure both computational efficiency and high accuracy, the total potential energy is primarily represented by the following potential energy terms [18]:

$$E_{\text{total}} = E_{\text{bonds}} + E_{\text{angles}} + E_{\text{dihedrals}} + E_{\text{nonbonded}} \quad (1)$$

In the equation, E_{total} represents the total potential energy of the system, measured in kcal/mol; E_{bonds} denotes bond energy; E_{angles} refers to angle energy; $E_{dihedrals}$ represents dihedral energy; and $E_{nonbonded}$ accounts for van der Waals interactions and other non-bonded interactions. The primary differences across the various molecular force fields lie in the functional forms and parameter expressions within the force field. For the OPLS force field, which is central to this study, each potential energy term can be expressed as follows:

$$E_{bonds^{\rho}} = \sum_{bonds^{\rho}} K_r (r - r_0)^2 \quad (2)$$

$$E_{angles^{\rho}} = \sum_{angles^{\rho}} K_\theta (\theta - \theta_0)^2 \quad (3)$$

$$E_{dihedrals} = \frac{c_1}{2}[1 + \cos(\varphi)] + \frac{c_2}{2}[1 + \cos(2\varphi)] + \frac{c_3}{2}[1 + \cos(3\varphi)] + \frac{c_4}{2}[1 + \cos(4\varphi)] \quad (4)$$

$$E_{nonbonded} = \sum_{i>j} \left\{ 4\varepsilon_{ij} f_{ij} \left[\left(\frac{\sigma_{ij}}{r_{ij}} \right)^{12} - \left(\frac{\sigma_{ij}}{r_{ij}} \right)^{6} \right] + \frac{q_i q_j e^2}{r_{ij}} \right\}, r < r_{cut} \quad (5)$$

In selecting force fields for this study, the CO_2 fluid phase is described using the transferable potential for phase equilibria (TraPPE) force field, which applies a rigid constraint on CO_2 molecules and excludes intramolecular interactions. Shale oil fluid is described using the optimized potentials for liquid simulations (OPLS) force field, which ensures a high computational accuracy while moderately improving simulation efficiency. The interaction parameters between different atom types are determined using the Lorentz–Berthelot mixing rule, with a cutoff radius of 1.2 nm. Long-range electrostatic forces are calculated using the particle-mesh Ewald (PME) method [19].

In the swelling model, three different concentrations of a CO_2 atmosphere are introduced around mixed alkane molecules, with CO_2 concentrations set at 1 K, 1.5 K, and 2 K based on the number of added CO_2 molecules, to investigate the swelling effects of varying CO_2 concentrations on the shale oil system. An additional model without a CO_2 atmosphere is included as a control group to evaluate the swelling effect of CO_2 on shale oil. The open-source software LAMMPS is used for simulation, with an initial 1 ns equilibrium simulation of the alkane mixture in the pore space under the NVT ensemble, while keeping the rock wall fixed, to emulate the actual presence of alkanes in reservoir pores. Following the introduction of the CO_2 atmosphere, molecular dynamics simulations are conducted for 2 ns for the entire system, with the temperature held at 330 K, a timestep of 1 fs, and data recorded every 1000 steps for analysis.

In the displacement model, a mixed alkane fluid is added to the left side of the slit pore, a CO_2 atmosphere is introduced on the same side, and a vacuum layer is applied to the right side of the slit to eliminate periodicity in the X-direction. Initially, the slit walls are fixed, and partitions are added to both sides of the mixed alkane fluid and CO_2 system. A 1 ns equilibrium simulation is conducted to simulate the adsorption state of the mixed alkanes in actual reservoir conditions. After reaching dynamic equilibrium, the restriction partition on the alkanes is removed, and a metal pressure plate is placed on the left side of the CO_2 system. Different displacement velocities are set for the pressure plate to drive CO_2 movement along the *X*-axis into the slit. The pressure plate velocities are set at 1 m/s, 2 m/s, 3 m/s, and 4 m/s, with the system temperature maintained at 330 K, a timestep of 1 fs, and data recorded every 1000 steps for analysis. Detailed component data are provided in Table 1.

Table 1. Statistics of component parameters in the displacement model.

Component	Temperature, K	Pressure, MPa	X, Å	Y, Å	Z, Å	Density, g/cm^3	Number of Molecules
Vacuum layer			40	40	60	-	-
CO_2			60		60	0.65	1500
C_4	330		-	-	-	0.66	140
C_{12}	40		-	-	-	0.73	100
C_{20}			-	-	-	0.75	80
α-SiO_2			80	40	10	-	-
$CaCO_3$			80	40	10	-	-

3. Results and Discussion

3.1. Mechanism of CO_2-Driven Oil Displacement in Quartz Reservoirs

3.1.1. Static Swelling Behavior

Following molecular dynamics simulations conducted using the LAMMPS software, data visualization and processing were performed in OVITO (version 2020) (Open Visualization Tool, a kind of scientific data visualization and analysis solution for particle-based simulations). Using CO_2 at a concentration of 1 K as an example, snapshot images were analyzed to observe the process. Over the course of the simulation, alkane molecules were progressively swollen by CO_2 molecules, gradually dispersing within the slit and forming a mixed-phase state with CO_2. As shown in Figure 3a, the mixed alkanes initially localized at the center of the slit gradually swelled and mixed with CO_2, eventually occupying the entire slit. Figure 3b reveals that by 30 ps, part of the C_4 components in the mixed alkanes had dissolved into the CO_2 phase. By 200 ps, it became apparent that some alkane molecules adsorbed on the wall surface were displaced by CO_2, which subsequently occupied portions of the rock wall previously adsorbed by alkanes. By the end of the simulation, the mixed alkanes and CO_2 had formed a near-complete mixed-phase state. Low molecular weight alkanes exhibited greater dispersion, whereas high molecular weight alkanes were more concentrated and adhered more closely to the rock wall. Furthermore, the high molecular weight alkanes demonstrated an extended configuration within the CO_2 environment [23,24].

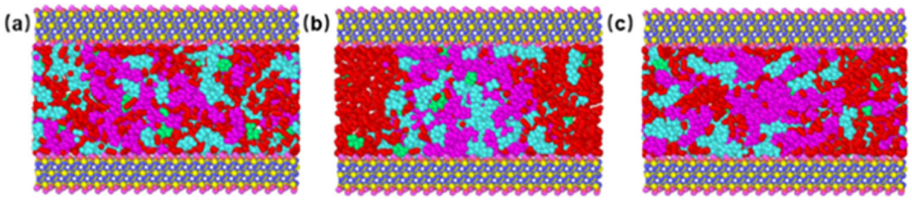


Figure 3. Swelling process evolution of the quartz model: (**a**) initial moment; (**b**) 30 ps; and (**c**) 200 ps. (Red: CO_2, green: C_4, blue: C_{12}, and purple: C_{20}).

During the simulation process, the interaction energies between the rock wall and the components within the fracture were statistically analyzed, with the results shown in Figure 4. The interaction energy between the rock wall and CO_2 is significantly higher than that of the alkane molecules, indicating that CO_2 molecules dominate in the competitive adsorption process with the rock wall. The overall interaction energy of shale oil is also lower than that of CO_2 molecules. The interaction energies of C_{12} and C_{20} with the rock wall are similar, but both are significantly higher than that of the C_4 molecules. Snapshot images further reveal that the distribution of C_4 is more dispersed, while C_{12} and C_{20} are located closer to the rock wall.

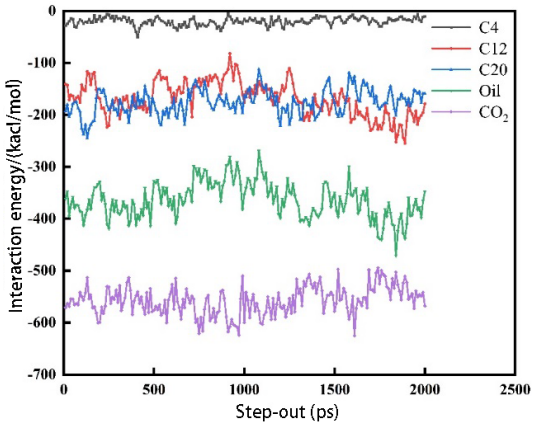


Figure 4. Interaction forces between molecules in the quartz fracture model.

During the simulation, the density distribution curves of each alkane component were also collected, as shown in Figure 5. From the figure, it can be observed that there are no multiple adsorption peaks for the alkane molecules. Instead, there is only a single adsorption peak at the wall surface, indicating that most of the alkane molecules were displaced from the wall by CO_2, forming a miscible state.

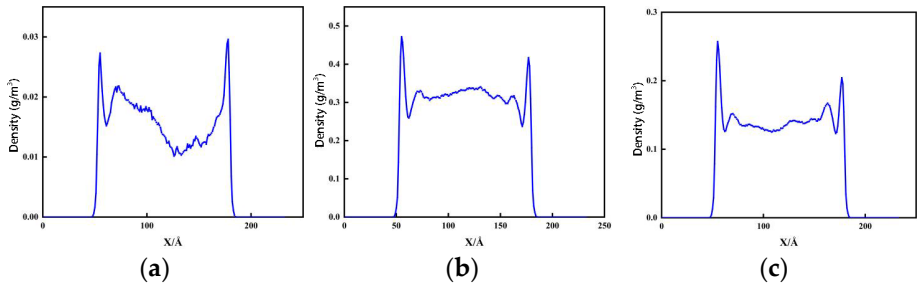


Figure 5. Density distribution of alkane molecules in the quartz slit model: (**a**) C_4; (**b**) C_{12}; and (**c**) C_{20}.

The density distribution curves of each component in atmospheres with different CO_2 concentrations are shown in Figure 6. From Figure 6a, it can be observed that as the CO_2 concentration increases, the peak density of CO_2 increases, although the shape of the curve remains largely unchanged. CO_2 is concentrated near the rock wall surface at all concentrations. For the mixed alkanes, as the CO_2 concentration increases, the concentration of alkane molecules surrounding the rock wall decreases. However, the distribution of alkane molecules shows little difference between concentrations of 1.5 K and 2 K.

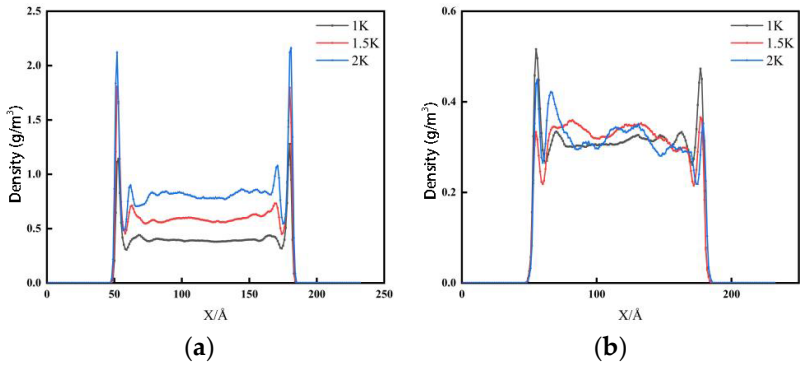


Figure 6. Density distribution of oil components and CO_2 in the quartz model under different CO_2 concentrations: (**a**) CO_2, and (**b**) oil.

3.1.2. Dynamic Displacement Process

Molecular dynamics simulations were conducted using the quartz fracture displacement model constructed earlier. The driving velocity of the metal plate on the left side was set at 1 m/s, 2 m/s, 3 m/s, and 4 m/s, and the molecular movement characteristics during the displacement process were recorded. The data on the density distribution of different molecules along the *X*-axis, interaction energies, and other parameters were analyzed to summarize the characteristics of CO_2 displacing alkanes in the quartz fracture and the effects of displacement velocity.

Figure 7 presents a schematic of the quartz fracture model at a displacement velocity of 1 m/s. During the displacement process, CO_2 molecules continually push the mixed alkane molecules forward, gradually displacing and stripping the molecules adsorbed on the pore wall surface. It can be observed from the figure that alkane molecules exhibit significant displacement in the X-direction over time. At the early stage of displacement, a depression forms in the center of the alkane molecules, and an oil film adsorption phenomenon can be observed on the left side of the fracture model. High molecular weight alkanes (C_{12} and C_{20}) adsorb on the pore wall surface, obstructing CO_2 movement along the wall, negatively impacting the internal displacement within the fracture. CO_2 continuously advances towards the center of the pore, and as it progresses, the distribution range of alkane molecules increases. From Figure 8, it can be observed that the alkane molecules on the left side are squeezed by CO_2, and the displacement front is continually broken through. Thus, a clear CO_2 breakthrough phenomenon is evident, indicating that the CO_2 in the center is in an ineffective displacement state.

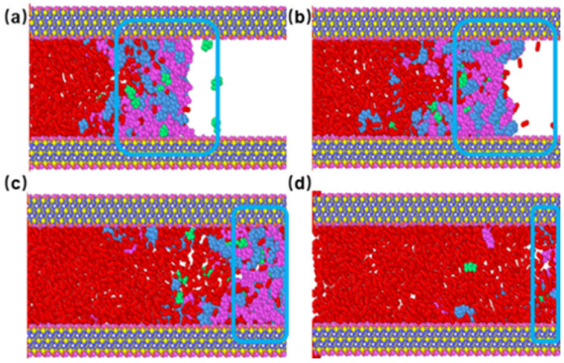


Figure 7. Schematic of the quartz fracture model at a displacement velocity of 1 m/s (red: CO_2, green: C_4, blue: C_{12}, and purple: C_{20}): (**a**) 1000 ps; (**b**) 3000 ps; (**c**) 7000 ps; and (**d**) 8000 ps.

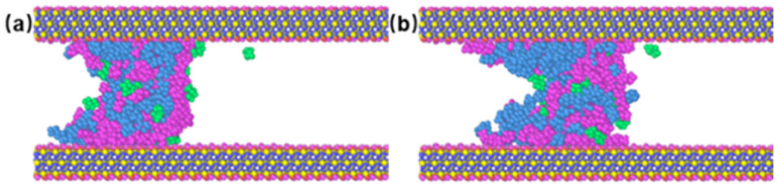


Figure 8. Fingering phenomenon of CO_2 during the displacement process in the quartz model (green: C_4, blue: C_{12}, and purple: C_{20}): (**a**) 1000 ps; and (**b**) 4000 ps.

Figure 9 presents the density distribution of each alkane in the fracture when the metal plate is moved closer to the rock wall. As the simulation time progresses, the density peak of the alkane molecules gradually shifts forward, indicating the formation of effective displacement behavior during the simulation. When comparing the displacement distances of different alkane molecules at the same time, C_4 exhibits the largest displacement, followed by C_{12}, and C_{20} shows the smallest displacement ($C_4 > C_{12} > C_{20}$). When the metal plate moves closer to the left side of the fracture wall, the density peaks of the alkane molecules

are primarily distributed near the nanopore exit, suggesting that during the simulation, CO_2 molecules have created an effective displacement process. Alkanes with different mass fractions exhibit relatively long displacement distances during the replacement process, resulting in effective displacement. However, compared to C_4, C_{12} and C_{20} show more residual presence in the pore. C_4 is almost entirely displaced by CO_2 out of the pore, while C_{12} and C_{20} show flatter density distributions within the pore, indicating the residual presence of C_{12} and C_{20}. Therefore, during the displacement process, CO_2 displaces C_4 more thoroughly, while C_{12} and C_{20} have a broader and richer distribution along the pore wall surface [25].

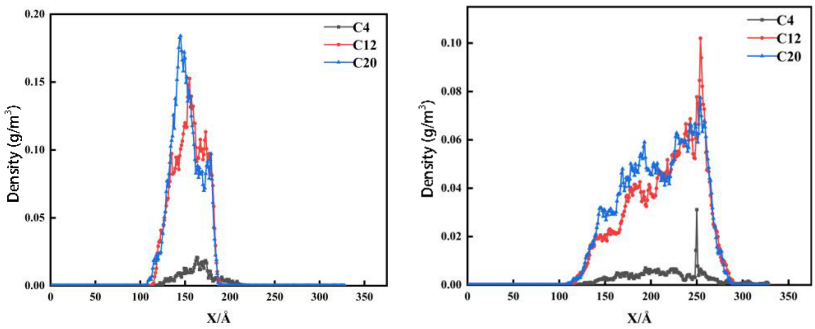


Figure 9. X-direction density distribution of each alkane component in the quartz model: (**a**) 100 ps, and (**b**) final state.

Figure 10 presents the interaction energy between alkanes and the rock wall surface, as well as the interaction energy between CO_2 and alkanes. The former reflects the adsorption strength between shale oil and the rock surface, where a greater interaction force indicates a more stable adsorption state. In cases where the interaction energy between shale oil and the rock wall is high, CO_2 has difficulty displacing and separating the alkanes adsorbed on the pore walls, thereby destabilizing the displacement interface. The latter primarily represents the miscibility between CO_2 and the shale oil components. A greater interaction energy between alkanes and CO_2 facilitates miscibility, enabling a miscible displacement process that stabilizes the displacement front. The adsorption strength of alkane molecules on the pore wall is relatively weak. During the displacement process, the interaction between CO_2 and alkanes plays a dominant role. After CO_2 displaces the alkanes from the slit, the reduced interaction between alkanes and CO_2 leads to the increase observed at the end of the curve in the simulation.

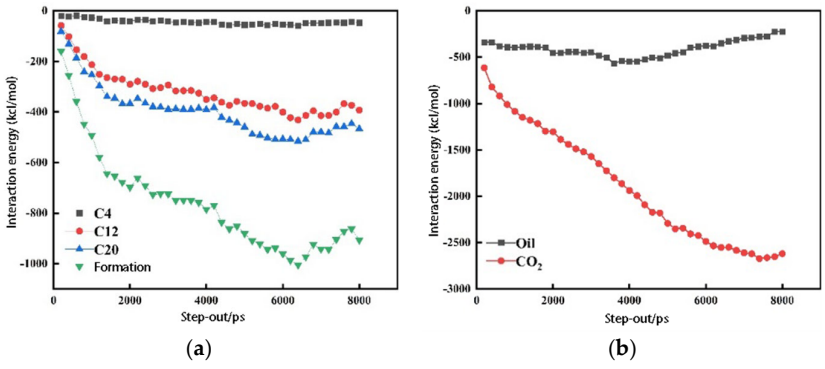


Figure 10. Interaction energy distribution: (**a**) interaction energy between CO_2 and each component; and (**b**) interaction energy between the quartz wall and each component.

3.1.3. Effect of Drive Velocity

Considering the significant impact of displacement velocity on the displacement effect, a series of molecular dynamics simulations were conducted at different CO_2 displacement velocities. The driving velocity of the metal plate was set to 1 m/s, 2 m/s, 3 m/s, and 4 m/s, respectively.

Figure 11 illustrates the final state of the slit model when the partition plate moves from its initial position to the region near the rock wall under different displacement velocities. At lower velocities, the alkanes are displaced over a longer distance, leading to more effective displacement. When the displacement velocity is 1 m/s, the alkanes in the pore are displaced the furthest, and the CO_2 phase in the pore dissolves more alkanes, indicating good miscibility between alkanes and CO_2, which facilitates CO_2 displacing shale oil. Similarly, it is observed that the distribution of C_{12} and C_{20} is more widespread and closer to the wall in the pore, reflecting that high molecular weight alkane molecules have a broader distribution, and the displacement in the X-direction is shorter. When the metal partition plate reaches the rock wall, alkane molecules in the pores with lower displacement velocities exhibit larger X-direction displacements compared to those in the pores with higher displacement velocities. This can be attributed to the fact that at a given displacement velocity, the increase in velocity results in a shorter contact time between CO_2 and alkanes, producing a stronger forward motion phenomenon. As a result, most of the CO_2 remains in an ineffective displacement state, leading to a reduction in the displacement efficiency [22].

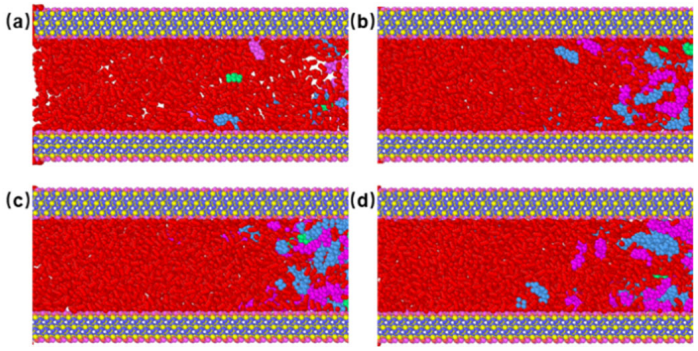


Figure 11. Schematic of final displacement results at different displacement velocities in the quartz model: (**a**) 1 m/s, (**b**) 2 m/s, (**c**) 3 m/s, and (**d**) 4 m/s (red: CO_2, green: C_4, blue: C_{12}, and purple: C_{20}).

Figure 12 presents the density distribution of alkanes in the X-direction at four different displacement velocities. It can be observed that, as the velocity decreases, the peak of the alkane density distribution appears farther along the X-direction. At a velocity of 1 m/s, the alkane molecules are distributed as far as 290 Å, while at 4 m/s, the distribution extends to only 260 Å. The distribution of C12 remains relatively widespread and abundant, showing a more extensive distribution at all four displacement velocities. Generally, lower displacement velocities favor the CO_2 displacement process, with the distribution range decreasing from 180 Å to 150 Å. As the displacement velocity increases, the displacement effect of CO_2 on alkanes weakens, resulting in a reduction in the X-direction displacement distance of the alkanes [22].

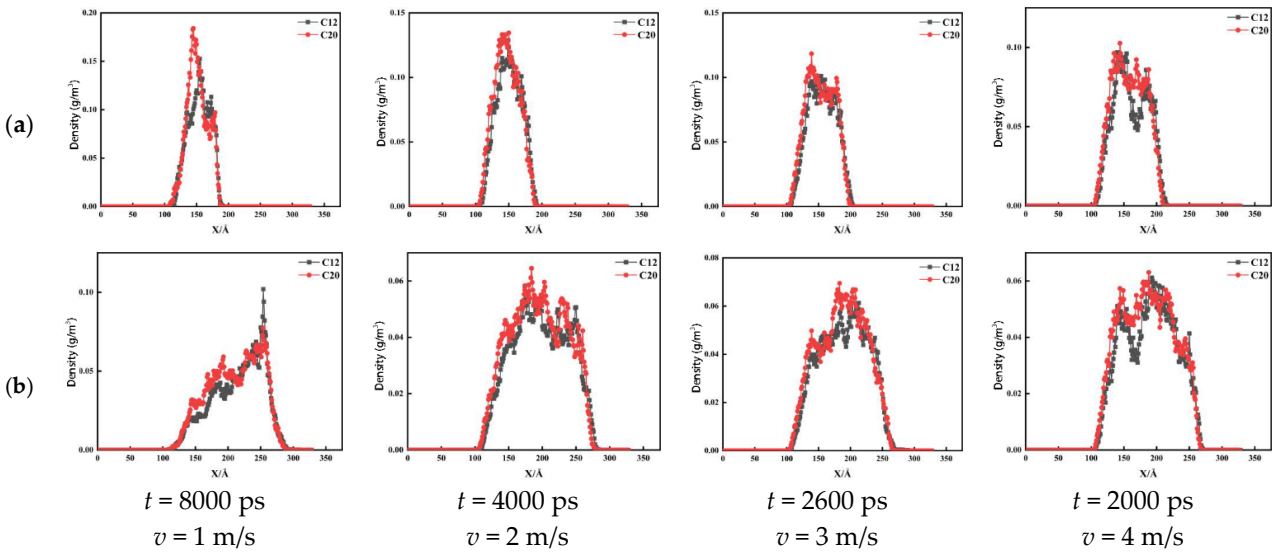


Figure 12. X-direction density distribution of alkane molecules at different displacement velocities in the quartz model ((**a**): t = 100 ps, and (**b**): t = final time).

3.2. Micro-Scale CO_2 Enhanced Oil Recovery Mechanism in the Calcite Reservoir

3.2.1. Static Swelling Behavior

For CO_2 at a concentration of 1 K, as the simulation progresses, alkane molecules are continuously swollen by CO_2 molecules, gradually dispersing within the slit and forming a mixed-phase state with CO_2, as shown in Figure 13. The mixed alkane molecules and CO_2 largely form a miscible phase, with low molecular weight alkanes more dispersed and high molecular weight alkanes more concentrated, presenting a more extended configuration. This result is consistent with that observed in the quartz slit system. However, in comparison to the quartz system, the distribution of alkane molecules in the calcite system is more concentrated over the same simulation time.

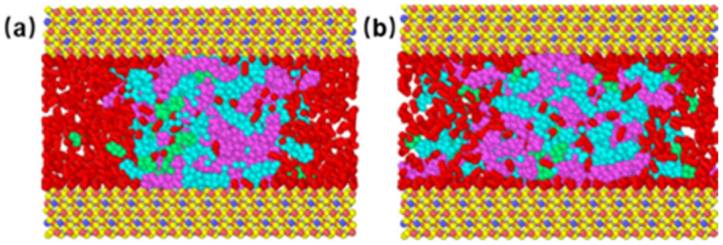


Figure 13. Swelling process evolution in the calcite model: (**a**) 30 ps; and (**b**) 200 ps. (Red: CO_2, green: C_4, blue: C_{12}, and purple: C_{20}).

The density distribution curves of each component under different CO_2 concentrations are shown in Figure 14. From the CO_2 curve, it can be observed that as the concentration increases, the peak density of CO_2 rises, but the shape of the curve remains relatively unchanged. For the mixed alkanes, as the CO_2 concentration increases, the concentration of alkane molecules around the rock wall decreases. However, the distribution of alkanes shows little variation between 1.5 K and 2 K, which is consistent with the results obtained from the quartz model.

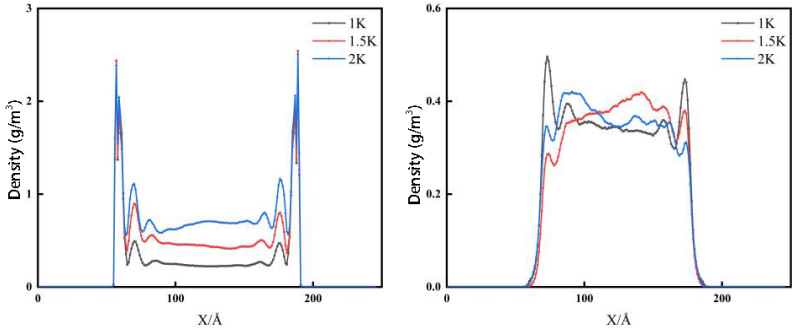


Figure 14. Density distribution of oil components and CO_2 in the calcite model under different CO_2 concentrations: (**a**) CO_2, and (**b**) oil.

3.2.2. Dynamic Displacement Process

Figure 15 presents snapshot diagrams of the calcite slit model under a displacement velocity of 1 m/s. These snapshots allow for a visual analysis of the displacement characteristics of each alkane molecule. CO_2 molecules continuously advance, displacing and peeling off alkane molecules adsorbed on the pore wall surface. In the early stages of displacement, depressions form between the alkane molecules, and an oil film adsorption phenomenon can be observed on the left side of the slit model. High molecular weight alkanes (C_{12} and C_{20}) adsorbed on the pore wall surface hinder the advancement of CO_2 along the wall and negatively affect the displacement of alkanes within the slit. CO_2 continues to advance towards the center of the pore, and as it progresses, the number of alkane molecules adsorbed on the alkane wall increases. From Figure 16, it is evident that the alkane molecules on the left side are compressed by CO_2, and the displacement front is progressively overcome. As a result, a clear forward motion (finger-like displacement) of CO_2 is observed, indicating that the CO_2 at the center of the pore is in an ineffective displacement state. Additionally, the finger-like displacement phenomenon observed in the calcite model is more pronounced than that in the quartz model, suggesting that more CO_2 molecules in the calcite model are in an ineffective displacement state.

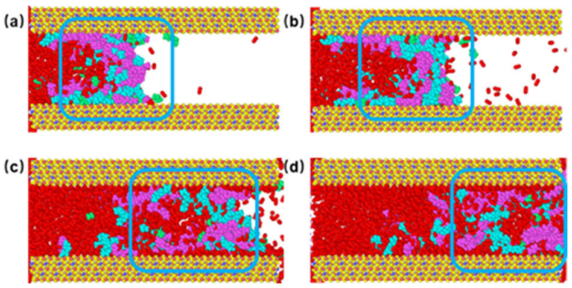


Figure 15. Snapshot of the calcite slit model at a displacement velocity of 1 m/s (red: CO_2, green: C_4, blue: C_{12}, and purple: C_{20}): (**a**) 1000 ps; (**b**) 3000 ps; (**c**) 7000 ps; and (**d**) 8000 ps.

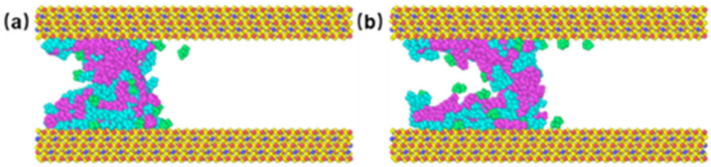


Figure 16. Finger-like displacement phenomenon of CO_2 during the displacement process in the calcite model (green: C_4, blue: C_{12}, and purple: C_{20}). (**a**) 1000 ps; and (**b**) 4000 ps.

Figure 17 illustrates the density distribution of different alkanes in the slit as the metal plate moves towards the rock wall. As the simulation progresses, the peak density of

the alkane molecules gradually shifts forward, indicating the formation of an effective alkane displacement phenomenon during the simulation. Specifically, when comparing the displacement of different types of alkane molecules at the same moment, it is found that C_4 has the largest displacement distance, followed by C_{12}, while C_{20} exhibits the smallest displacement distance ($C_4 > C_{12} > C_{20}$). When the metal plate approaches the left wall of the slit, the peak density of all alkane molecules is primarily concentrated near the outlet of the nanopore. This indicates that CO_2 molecules have effectively driven the movement of alkane molecules during the simulation, achieving the significant displacement of alkanes with different mass fractions and resulting in effective replacement. However, compared to C_4, C_{12} and C_{20} have more residuals in the pore; C_4 is almost completely displaced by CO_2 from the pore, while C_{12} and C_{20} exhibit relatively stable density distributions in the pore, indicating their residual presence. Therefore, it can be observed that CO_2 exhibits better displacement efficiency for C_4, while C_{12} and C_{20} are more widely distributed and more abundant on the pore wall, with the results consistent with those observed in the quartz wall model.

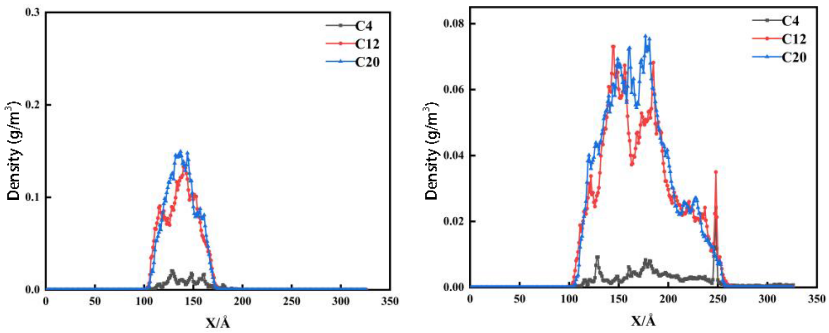


Figure 17. X-direction density distribution of alkane components in the calcite model: (**a**) 100 ps, and (**b**) 8000 ps (final).

3.2.3. Effect of Drive Velocity

Considering the significant impact of displacement velocity on the displacement effect, a series of molecular dynamics simulations were conducted to vary the CO_2 displacement velocity. The displacement velocity of the metal plate was set at 1 m/s, 2 m/s, 3 m/s, and 4 m/s, respectively.

Figure 18 presents the final state of the slit model as the separator moves from its initial position towards the rock wall under different displacement velocities. It can be observed that at lower velocities, alkanes are displaced over a greater distance, showing better displacement performance. Specifically, at a displacement velocity of 1 m/s, the alkane displacement distance in the pore is the greatest. Additionally, CO_2 in the pore dissolves more alkanes, indicating a good miscibility between alkanes and CO_2, which facilitates the replacement of shale oil by CO_2. Furthermore, it was observed that in the pore, the distribution of C_{12} and C_{20} is more widespread and closer to the wall, reflecting that high molecular weight alkanes have a broader distribution, with shorter displacements in the X-direction.

As the displacement velocity increases, when the metal separator moves closer to the rock wall, the displacement of alkane molecules in the pore in the X-direction is larger at lower velocities. It is speculated that under a given displacement velocity, as the velocity increases, the contact time between CO_2 and alkanes is reduced, resulting in a stronger finger-like displacement phenomenon, causing most CO_2 to be in an ineffective displacement state, which in turn reduces the displacement effect. Simultaneously, the

finger-like displacement phenomenon in the calcite system becomes more pronounced as the displacement velocity increases, leading to a poorer final displacement effect.

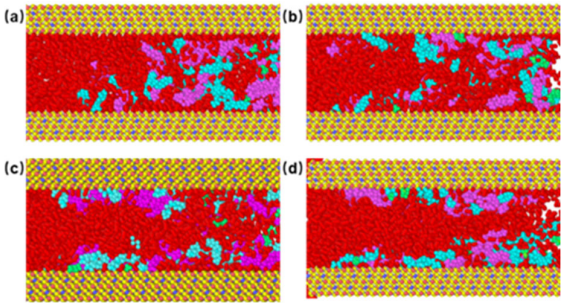


Figure 18. Schematic of final displacement results at different displacement velocities in the calcite model: (**a**) 1 m/s, (**b**) 2 m/s, (**c**) 3 m/s, (**d**) 4 m/s (red: CO_2, green: C_4, blue: C_{12}, and purple: C_{20}).

Figure 19 illustrates the density distribution of alkane molecules in the X-direction at four different displacement velocities. It can be clearly observed that as the displacement velocity decreases, the peak position of the alkane molecule density distribution in the X-direction shifts further, indicating a more widespread and concentrated distribution of alkanes at lower velocities. The distribution of C_{12} and C_{20} at all velocities shows a broader spread. In general, lower displacement velocities are more favorable for the CO_2 displacement process. However, as the displacement velocity increases, the ability of CO_2 to displace alkanes weakens, leading to a shorter displacement distance of alkanes in the X-direction, which is consistent with the findings in the quartz model.

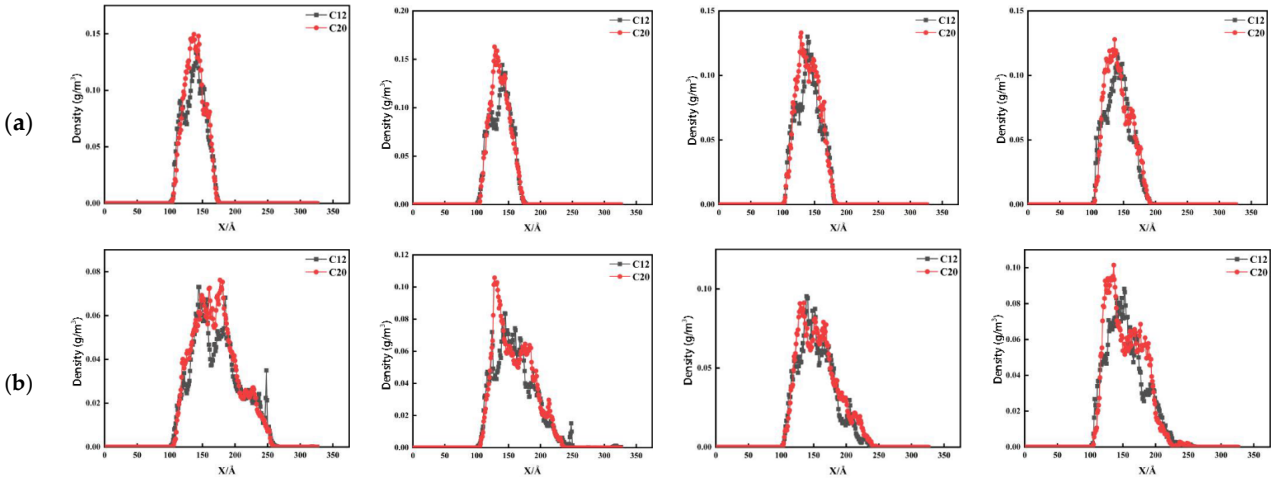


Figure 19. X-direction density distribution of alkane molecules at different displacement velocities in the calcite model. ((**a**): t = 100 ps, (**b**): t = final time).

4. Conclusions

(1) During the static swelling process, as the simulation time progresses, alkane molecules are continuously swollen by CO_2 molecules, gradually dispersing in the nanospace and forming a miscible phase with CO_2. Low molecular weight alkanes are more dispersed, while high molecular weight alkanes are more concentrated, with their distribution more closely aligned with the rock surface, exhibiting a more extended state in CO_2. The interaction energy between the rock surface and CO_2 is significantly greater than that between the alkane molecules, making CO_2 molecules dominate in the competition for adsorption on the rock surface.

(2) During the dynamic displacement process, alkane molecules exhibit noticeable displacement in the X-direction over time. High molecular weight alkanes (C_{12} and C_{20}) adsorb on the pore wall surfaces, hindering the forward movement of CO_2 along the pore walls, which negatively impacts the displacement of alkanes within the nanopores. CO_2 continuously advances from the pore center, and the CO_2 finger phenomenon becomes evident, with CO_2 at the pore center in an ineffective displacement state. During displacement, C_4 experiences the greatest displacement in the X-direction, followed by C_{12}, and C_{20} experiencing less displacement ($C_4 > C_{12} > C_{20}$). CO_2 displaces C_4 more effectively, while C_{12} and C_{20} are more widely distributed and richer on the pore wall surface.

(3) CO_2 molecules dominate the competitive adsorption with the rock surface, with their interaction energy significantly higher than that of alkane molecules. At lower displacement velocities, alkane molecules can move further in the X-direction. As the displacement velocity increases, the contact time between CO_2 and alkanes decreases, leading to intensified fingering phenomena, with most of the CO_2 in an ineffective displacement state, thereby reducing the displacement efficiency. This effect is more pronounced in the calcite model, indicating that more CO_2 molecules are in an ineffective displacement state. In the CO_2 displacement of shale oil, controlling the appropriate displacement velocity is crucial for optimizing the displacement effectiveness. Low-speed displacement is conducive to enhancing alkane mobility and displacement efficiency, while high-speed displacement may reduce efficiency due to fingering effects and decreased effective contact time.

Author Contributions: Conceptualization, C.L., Z.X. and H.X.; methodology, F.Y. and J.Y.; software, J.Y.; validation, L.R. and J.Y.; formal analysis, T.H., C.J. and C.L.; investigation, H.X., F.Y. and C.L.; data curation, J.Y., H.X. and F.Y.; writing—original draft preparation, J.Y., H.X. and F.Y.; writing—review and editing, J.Y. and Z.W.; supervision, Z.W. All authors have read and agreed to the published version of the manuscript.

Funding: This study was funded by the National Natural Science Foundation of China (Grant No. 52404046), the Hubei Province Natural Science Foundation Joint Fund Project (Grant No. 2024AFD385), and the Wuhan Municipal Science and Technology Bureau Shuguang Program Special Project.

Data Availability Statement: The original contributions presented in the study are included in the article, and further inquiries can be directed to the corresponding author.

Conflicts of Interest: Author Chengshan Li, Hongbo Xue, Liping Rao, Fang Yuan, Zhongyi Xu, Tongtong He and Chengwei Ji were employed by the China National Petroleum Corporation. The remaining authors declare that the research was conducted in the absence of any commercial or financial relationships that could be construed as a potential conflict of interest.

References

1. Wu, B.; Wu, C.; Tan, Q.; Chu, Y.; Liang, C.; Li, W.; Zhang, J.; Chen, Y.; Xu, T.; Wang, L. Accumulation conditions and key technologies for exploration and development of Changji shale oil in Jimusar sag of Junggar Basin. *Acta Pet. Sin.* **2024**, *45*, 437–460.
2. Li, Q.; Li, Q.; Han, Y. A Numerical Investigation on Kick Control with the Displacement Kill Method during a Well Test in a Deep-Water Gas Reservoir: A Case Study. *Processes* **2024**, *12*, 2090. [CrossRef]
3. Alfarge, D.; Wei, M.; Bai, B. Factors affecting CO_2-EOR in shale-oil reservoirs: Numerical simulation study and pilot tests. *Energy Fuels* **2017**, *31*, 8462–8480. [CrossRef]
4. Jin, L.; Hawthorne, S.; Sorensen, J.; Pekot, L.; Kurz, B.; Smith, S.; Heebink, L.; Herdegen, V.; Bosshart, N.; Torres, J.; et al. Advancing CO_2 enhanced oil recovery and storage in unconventional oil play-Experimental studies on Bakken shales. *Appl. Energy* **2017**, *208*, 171–183. [CrossRef]
5. Sheng, J. Critical review of field EOR projects in shale and tight reservoirs. *J. Pet. Sci. Eng.* **2017**, *159*, 654–665. [CrossRef]
6. Jia, B.; Tsau, J.S.; Barati, R. A review of the current progress of CO_2 injection EOR and carbon storage in shale oil reservoirs. *Fuel* **2019**, *236*, 404–427. [CrossRef]

7. Song, Z.; Song, Y.; Li, Y.; Bai, B.; Song, K.; Hou, J. A critical review of CO_2 enhanced oil recovery in tight oil reservoirs of North America and China. *Fuel* **2020**, *276*, 118006. [CrossRef]
8. Liu, H.; Tao, J.; Meng, S.; Li, D.; Cao, G.; Gao, Y. Application and prospects of CO_2 enhanced oil recovery technology in shale oil reservoir. *China Pet. Explor.* **2022**, *27*, 127–134.
9. Su, Y.; Wang, H.; Zhan, S.; Wang, W.; Xu, J. Research progress on characterization and simulation of shale oil flow in microscale. *J. Shenzhen Univ. Sci. Eng.* **2021**, *38*, 579–589. [CrossRef]
10. Wang, S.; Feng, Q.; Zha, M.; Lu, S.; Qin, Y.; Xia, T.; Zhang, C. Molecular dynamics simulation of the occurrence state of liquid alkanes in shale organic matter pores and fractures. *Pet. Explor. Dev.* **2015**, *42*, 772–778. [CrossRef]
11. Wang, X.; Chen, J.; Ren, D. Research progress and prospect of pore structure representation and seepage law of continental shale oil reservoir. *Pet. Reserv. Eval. Dev.* **2023**, *13*, 23–30.
12. Hong, X.; Xu, H.; Cui, F.; Yu, H.; Wu, Y.; Wu, H.; Wang, F. Application of molecular simulation in unconventional oil and gas development. *Chin. J. Comput. Mech.* **2021**, *38*, 313–320.
13. Zhang, Y.; Li, D.; Xin, G.; Ren, S. Molecular insights into recovery of shale gas by injecting CO_2-rich industrial waste gas in kerogen slit nanopores. *Gas Sci. Eng.* **2023**, *115*, 205025. [CrossRef]
14. Sun, J.; Chen, Z.; Wang, X.; Zhang, Y.; Qin, Y.; Chen, C.; Li, W.; Zhou, W. Displacement characteristics of CO_2 to CH_4 in heterogeneous surface slit pores. *Energy Fuels* **2023**, *37*, 2926–2944. [CrossRef]
15. Perez, F.; Devegowda, D. A molecular dynamics study of soaking during enhanced oil recovery in shale organic pores. *SPE J.* **2020**, *25*, 832–841. [CrossRef]
16. Santos, M.S.; Franco, L.F.; Castier, M.; Economou, I. Molecular dynamics simulation of *n*-Alkanes and CO_2 confined by calcite nanopores. *Energy Fuels* **2018**, *32*, 1934–1941. [CrossRef]
17. Wang, H.; Su, Y.; Wang, W.; Jin, Z.; Chen, H. CO_2-oil diffusion, adsorption and miscible flow in nanoporous media from pore-scale perspectives. *Chem. Eng. J.* **2022**, *450*, 137957. [CrossRef]
18. Chen, H.; Wu, Z.; Jiang, S.; Chen, Z. Mechanism of CO_2/N_2 oil exchange in tight reservoirs based on molecular dynamics simulation. *Bull. Geol. Sci. Technol.* **2024**, 1–14. [CrossRef]
19. Wu, Z.; Sun, Z.; Shu, K.; Jiang, S.; Gou, Q.; Chen, Z. Mechanism of shale oil displacement by CO_2 in nanopores: A molecular dynamics simulation study. *Adv. Geo-Energy Res.* **2024**, *11*, 141–151. [CrossRef]
20. Dong, X.; Xu, W.; Liu, H.; Chen, Z.; Lu, N.; Wang, W. On the replacement behavior of CO_2 in nanopores of shale oil reservoirs: Insights from wettability tests and molecular dynamics simulations. *Geoenergy Sci. Eng.* **2023**, *223*, 211528. [CrossRef]
21. Dong, X.; Xu, W.; Liu, R.; Chen, Z.; Lu, N.; Guo, W. Insights into adsorption and diffusion behavior of shale oil in slit nanopores: A molecular dynamics simulation study. *J. Mol. Liq.* **2022**, *22*, 359. [CrossRef]
22. Dong, X.; Xu, W.; Liu, H.; Chen, Z.; Lu, N. Molecular insight into the oil displacement mechanism of CO_2 flooding in the nanopores of shale oil reservoir. *Pet. Sci.* **2023**, *20*, 3516–3529. [CrossRef]
23. Wang, L.; Zhang, Y.; Liu, Y.; Huang, L.; Zou, R.; Meng, Z.; Lei, H. Molecular dynamics analysis on occurrence characteristics of shale oil and competitive adsorption mechanism of CO_2 and oil. *J. China Univ. Pet. Ed. Nat. Sci.* **2023**, *47*, 128–136.
24. Zhang, Y.; Wang, L.; Zou, R.; Zou, R.; Meng, Z.; Huang, L.; Liu, Y.; Lei, H. Effect of cosolvents on CO_2 displacement of shale oil and carbon storage. *Pet. Explor. Dev.* **2023**, *50*, 1318–1326. [CrossRef]
25. Ren, X.; Wang, J.; Dong, H.; Sheng, P.; Xu, H.; Zhang, H. Molecular simulation of CO_2 huff and puff effects in tight oil considering component differences. *Fault-Block Oil Gas Field* **2022**, *29*, 229–233.

Disclaimer/Publisher's Note: The statements, opinions and data contained in all publications are solely those of the individual author(s) and contributor(s) and not of MDPI and/or the editor(s). MDPI and/or the editor(s) disclaim responsibility for any injury to people or property resulting from any ideas, methods, instructions or products referred to in the content.